

Analytical Versus Voxelized Phantom Representation for Monte Carlo Simulation in Radiological Imaging

Jörg Peter*, *Member, IEEE*, Martin P. Tornai, *Member, IEEE*, and Ronald J. Jaszczak, *Fellow, IEEE*

Abstract—Monte Carlo simulations in nuclear medicine, with accurately modeled photon transport and high-quality random number generators, require precisely defined and often detailed phantoms as an important component in the simulation process. Contemporary simulation models predominantly employ voxel-driven algorithms, but analytical models offer important advantages. We discuss the implementation of ray-solid intersection algorithms in analytical superquadric-based complex phantoms with additional speed-up rejection testing for use in nuclear medicine imaging simulations, and we make comparisons with voxelized counterparts. Comparisons are made with well-known cold rod:sphere and anthropomorphic phantoms. For these complex phantoms, the analytical phantom representations are nominally several orders of magnitude smaller in memory requirements than are voxelized versions. Analytical phantoms facilitate constant distribution parameters. As a consequence of discretizing a continuous surface into finite bins, for example, time-dependent voxelized phantoms can have difficulties preserving accurate volumes of a beating heart. Although virtually no inaccuracy is associated with path calculations in analytical phantoms, the discretization can negatively impact the simulation process and results. Discretization errors are apparent in reconstructed images of cold rod:sphere voxel-based phantoms because of a redistribution of the count densities in the simulated objects. These problems are entirely avoided in analytical phantoms. Voxelized phantoms can accurately model detailed human shapes based on segmented computed tomography (CT) or magnetic resonance imaging (MRI) images, but analytical phantoms offer advantages in time and accuracy for evaluation and investigation of imaging physics and reconstruction algorithms in a straightforward and efficient manner.

Index Terms—Analytical phantoms, discretization, Monte Carlo methods, PET, SPECT, voxelized phantoms.

I. INTRODUCTION

COMPUTER-based Monte Carlo simulations can be exploited to investigate several clinically significant physical and technological aspects of radiological imaging [1]–[3]. Simulations of nuclear medicine systems can provide a statistically accurate estimate of the photon transport problem within arbitrarily complex isolated points or distributed objects in various media, and they are especially useful for those problems that cannot be solved analytically. Hence, the simulation results

can be used to understand the physics of the image formation process [4], [5]. For tomographic nuclear emission techniques such as single photon emission computed tomography (SPECT) and positron emission tomography (PET), Monte Carlo simulated projection data can be used to evaluate compensation techniques incorporated in novel reconstruction algorithms [6]–[9].

Limitations of Monte Carlo simulation include the enormous demand on computer memory (phantom data; working arrays, projected data, frequently allocated for several energy windows or scatter orders) and computation time (often measured in hours for a complete projection set). Because Monte Carlo solves the transport problem by generating a very large number of photon trajectories (often more than 10^5 histories per projection angle), the geometric representation of activity and material distributions (e.g., a complex phantom), which affects both performance parameters, is a critical component of the simulation setup as well as its performance. With the application of four-dimensional (4-D) (x, y, z, t) phantoms to investigate time-gated imaging techniques, phantom-related aspects become even more intensive. On the other hand, continually improving computer performance reduces computation costs and facilitates more widespread use of Monte Carlo methods for various imaging problems. In spite of the hardware platform being used, effective Monte Carlo methods almost always incorporate variance reduction techniques [10], [11] or, as recently proposed by Beekman *et al.* [12], for instance, employ simulation methods based on correlated photon tracking and convolution-based forced detection that markedly improve computational efficiency. Concerning the Poisson nature of the activity distributions in SPECT and PET, variance reduction or other approximations may result in statistically relevant deviations from an otherwise unbiased simulation result because Monte Carlo simulated projections are (in consequence of variance reduction) not count but probability data. The Monte Carlo code used for simulations in this paper has been carefully evaluated with regard to this aspect, and the desired Poisson statistics is preserved by appropriate rescaling the projected probabilities into counts. It is assumed also that the underlying physics and quality of the applied random number generator are accurate and efficient.

As we evaluate and compare the voxelized and analytic phantom representations commonly used for simulation purposes in nuclear medicine, it becomes apparent that computational performance is affected by the object description, and more importantly, the accuracy of the simulation result may vary. Voxelized phantoms, derived either from segmented tomographic data [13], [14] or from mathematically defined geometric models that are discretized afterward [15], [16]

Manuscript received August 30, 1999; revised February 9, 2000. This work was supported by PHS, under Grants R01-CA33541 and R01-CA76006, the National Institute of Health, and the Department of Energy, under Grant DE-EG02-96ER62150. The Associate Editor responsible for coordinating the review of this paper and recommending its publication was F. J. Beekman. *Asterisk indicates corresponding author.*

The authors are with Duke University Medical Center, Durham, NC 27710 USA (e-mail: peter@dec3.mc.duke.edu).

Publisher Item Identifier S 0278-0062(00)05314-3.

can be applied to voxel-based ray-tracing algorithms, such as proposed by Siddon [17]. On the other hand, “true” analytical phantoms [18], [19] are specified by parameters of equations that model the phantom objects and require appropriate algorithms to calculate photon ray-phantom object intersections. Tomographic phantoms obtained from segmented X-ray computed tomography (CT) or magnetic resonance imaging (MRI) images [13], [14] provide highly realistic physical simulations in their complexity. Analytical phantoms, in contrast, span simple geometries such as point or cylindrical phantoms to more complex anthropomorphic phantoms, e.g., the mathematical cardiac torso (MCAT) phantom [15], [20] and the superquadric-based thorax phantom recently proposed by the authors [19], [21]. These analytical phantoms are appropriate for investigating and evaluating new imaging geometries or reconstruction algorithms because they are based on exactly defined, regularly shaped, continuous objects. Furthermore, anthropomorphic mathematical phantoms can be easily modified to mimic anatomical variability encountered clinically.

The advantage in accuracy of analytically defined versus voxelized phantoms, however, is often not preserved during simulation. For example, the MCAT phantom is defined mathematically and has all of the features of an analytical phantom, but is predominantly used in its discretized representation in simulations [7], [22]–[24]. As a result, the continuous properties of this phantom are lost because it is used like a voxelized phantom. One reason for this may be founded in the fact that Monte Carlo programs commonly used in nuclear medical imaging (a survey and description of key features can be found in [3]) model photon transport through voxel-based phantoms. Solving the ray-tracing problem through (simple geometric) shape-based phantoms has been implemented only in a few codes [3]; none of these simulates phantom models with more complex (higher order) interprimitive relationships. This disproportion in part reflects the very high costs in developing and maintaining a Monte Carlo program. Nevertheless, the complex phantom represents a crucial component of the probability distribution function for simulation, and as will be shown here, degrading the quality of mathematically defined phantoms by discretization seems to be equally expensive.

In radiological imaging, the first Monte Carlo approach to calculate the intersections of photon rays with phantom structures, while preserving the geometric shape parameters in an analytical anthropomorphic phantom model, was proposed by Wang *et al.* [18], [25], [26]. Within this composite model, basic solids (e.g., ellipsoid, elliptical cylinder, tapered elliptical cylinder, rectangular solid, and their hemi, quarter, and octal sections) as well as Boolean combinations of solids such as union or intersection are used to model complex phantom objects. An inclusion tree approach was used in this code to describe interprimitive relationships providing information about inclusion relationships among phantom objects. For the Monte Carlo code used in this investigation, we extended the phantom models used previously and generalized the analytical quadric-based phantoms by employing closed superquadric surfaces (formulated as superellipsoids and supertoroids) that best fit the need for an efficiently modeled anthropomorphic phantom. These superquadrics are also easily used if

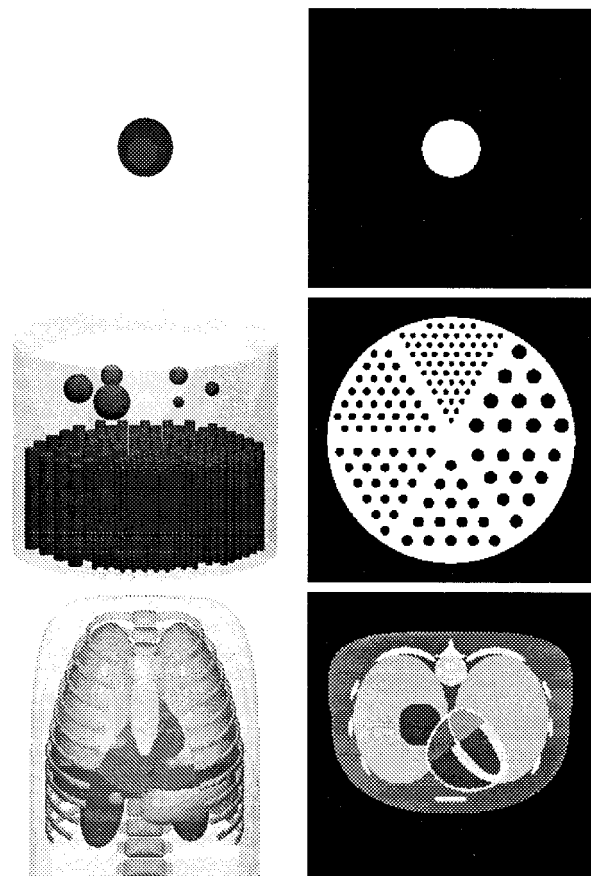


Fig. 1. Rendered views of analytically defined phantoms (left column) and transverse images of their voxelized counterparts (256^3 voxels, right column). Top row: single sphere; middle row: cold rod : sphere phantom (160 simploids); bottom row: superquadric-based anthropomorphic thorax phantom (86 simploids).

simple-geometric phantoms are required. In addition, simulations can also be performed on voxelized phantoms or phantom inserts of any size and arbitrary combination with analytical phantoms or inserts, whereby physical simulation parameters (modeled probability distribution, imaging geometry, random number generator seed, number of photon histories, scatter order) can be defined identically for all phantom representations.

II. PHANTOM REPRESENTATION

In order to evaluate analytical versus voxelized phantoms in Monte Carlo simulations of radiological imaging systems, specifically, SPECT, the phantoms shown in Fig. 1 have been analytically modeled (left column) and afterward discretized into 128^3 (not shown) and 256^3 (right column) voxels, respectively. We have chosen these grid sizes for practical reasons that reflect the most commonly used spatial dimensions to be found in simulating SPECT systems; analytical phantoms can in fact be discretized into any arbitrary number of voxels. Two complex phantoms we investigate include a cold rod : sphere phantom (modeled on the ECT/DLX/P phantom from Data Spectrum Corp., Hillsborough, NC) and an anatomically correct anthropomorphic torso.

TABLE I
MEMORY DEMAND OF THE 3-D/4-D ANTHROPOMORPHIC CARDIAC TORSO
PHANTOM IN kBytes (UNCOMPRESSED)

| | Analytic | 128 ³ | 256 ³ |
|---------------------|----------|------------------|------------------|
| 3D | 12 | 2,048 | 16,384 |
| 4D (16 time frames) | 64 | 32,786 | 262,144 |

After discretizing the analytically defined phantoms, the immediate observation concerns the explosion of memory demand. Table I shows the uncompressed amount of memory necessary to allocate the data of the analytical anthropomorphic thorax phantom as well as its voxelized representations (1 byte per voxel is appropriate for phantoms with up to 256 geometric shapes). At least during simulation, 16 MBytes of phantom data have to be allocated for both three-dimensional (3-D) and 4-D discretized phantom representations with 256³ voxels. In contrast, only 0.36% of this memory is necessary for the exact 4-D analytical phantom that also includes information about inclusion relationships between phantom objects. As a practical consequence of this, simulations performed with analytical phantoms require less-expensive hardware configurations. For the anthropomorphic phantom, the size of the volume to be discretized has been chosen to be 45 cm³, whereby the torso vertical length is 44.5 cm. This results in 3.52-mm and 1.76-mm spatial image resolution for 128³ or 256³ phantom voxels, respectively. On the contrary, resolution of analytical phantoms is limited only by precision of the data type used ($<10^{-24}$ for double precision). Spatial resolution of the voxelized cold rod: sphere phantom is 1.95 mm and 0.98 mm corresponding to 128³ or 256³ voxels, respectively.

III. DISCRETIZATION ERRORS

It is well known that the process of discretizing an analytically defined surface inevitably leads to errors because a continuous surface is essentially truncated into a finite number of bins. In the following subsections, we will describe two discretization problems within the context of Monte Carlo simulation that we observed to have significant consequences on the quality of the simulation result.

A. Alteration of Associated Distribution Parameters

The loss of structural information is the most obvious problem encountered after discretization. Structural alterations, subsequently, also quantitatively change the associated piecewise uniform distribution of those material-specific source activities, or other relevant parameters by which the phantom object is characterized.

For example, assume a point source has to be modeled with 2.0-mm diameter, as part of a phantom whose outer square size is 40.0 cm. Discretizing this space into 128³ and 256³ voxelized representations, respectively, will transform this spherical source into a rectangular source occupying a single voxel in both cases. The square size of this cubical source is 3.13 mm if discretized into 128³ voxels and 1.56 mm for 256³ voxels. Besides the dramatic change in shape, the volume of the source

TABLE II
DISCRETIZATION ERRORS FOR A 2.0-mm POINT SOURCE INTO 3.13-mm AND
1.56-mm VOXELS FOR 128³ AND 256³ ARRAYS, RESPECTIVELY, AFFECTING
ACTIVITY CONCENTRATION AND DISTRIBUTION

| | Analytic | 128 ³ | 256 ³ |
|---------------------------|----------|------------------|------------------|
| volume (mm ³) | 4.19 | 30.67 | 3.80 |
| error (%) | — | 632.01 | -9.31 |

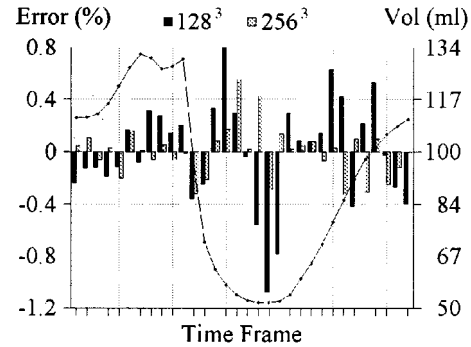


Fig. 2. Deviation of measured voxelized left ventricular blood volume from analytical model for 32 time frames. In the case of the 128³ phantom, the error can be greater than 1% with respect to the time frame volume. Bars represent percent error for the given voxel size; the superimposed solid line represents the left ventricular blood volume curve for one cardiac cycle.

changes even more markedly (Table II). Although in this example geometric modifications of regions are not possible (except by altering the resolution to further minimize volume deviation), based on the remeasured source volumes of the voxelized phantoms, the distribution parameter value associated with the phantom object can be adjusted.

The next example illustrates the same problem in the context of designing a 4-D cardiac phantom insert [21]. In this case, the radii in x , y , z directions of the hemi-ellipsoid modeling the cavity of the left ventricle [see Fig. 3(a) for geometry] have been defined such that the volume of the solid equals measured left ventricular blood volume values. Solving this measured volume-modeled shape relationship at certain times during a cardiac cycle results in the contraction pattern of the modeled cavity. The modeled volume relationship is absolutely preserved in the analytically defined phantom. It is, however, only approximated with discretization. Fig. 2 shows the deviation of the measured voxelized left ventricular cavity volumes from that analytical model. Of course, similar error patterns are involved in any voxelized approximation of modeled functional relationships. Modeling constant myocardium volume during cardiac cycle can hardly be accurately preserved by a voxelized phantom. Although in this example reassignment modifications of voxels to regions are possible to minimize the error, we quickly diverge into solving a multivariate optimization problem.

B. Inaccuracy of Photon Path Calculations

As a direct result of the approximation of continuous surfaces described in the previous subsection, a closed homogeneous representation of regions is not guaranteed. Examples of this problem are shown in Fig. 3. These errors not only degrade

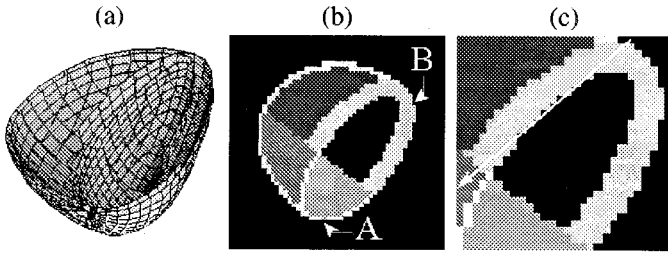


Fig. 3. (a) Sectional view of the analytically defined superquadric-based cardiac insert. (b) Possible artifacts because of discretization: (A) closed region becomes disconnected; (B) sudden change of region thickness. (c) Illustration of inaccurate photon path calculation (voxel size: 128^3).

simulation quality, but also may result in slower simulation execution and unexpected behavior of the Monte Carlo code being used, especially at activity or material interfaces. The evolved error indicated by (B) in Fig. 3(b)—thinning of the myocardium wall because of discretization occurring near the apex region of the heart—could be seen as an additional factor affecting the problem of slightly decreased activity of the apical region [27] when studies are performed on voxelized phantom data. An example of inaccurate photon path calculation during simulation is shown in Fig. 3(c). Whereas the indicated photon ray intersects the myocardium four times in the analytical phantom model, which would represent the real conditions, in this scenario, 18 intersections were found instead.

It should be noted that the described discretization errors are not the sole errors encountered in Monte Carlo simulations. However, they are the first involved within the unavoidable chain of systematic error propagation. All examples in this section illustrate that errors caused by discretization are of an especially serious nature for phantoms containing fewer voxels. Depending on the complexity of the phantom, finer spatial resolution of the discretized phantom yields smaller discretization errors. However, finer phantom resolutions, i.e., a greater number of phantom voxels for which the radiological path has to be solved per photon history, obviously results in slower simulation execution.

IV. COMPUTATIONAL SPEED

Monte Carlo simulation is a very time-consuming method of solving integral equations. One of the most expensive parts of Monte Carlo simulation in radiological imaging—as this is true likewise for the exact calculation of the radiological path in iterative reconstruction algorithms—is the calculation of the intersections of the photon path with the boundaries of the phantom objects. For voxelized phantoms, those boundaries are defined by planes that enclose the voxel elements. Boundaries of objects in analytical phantoms are defined by the implicit equations of the surfaces that define those objects. In general, analytical phantoms consist of a much smaller number of objects than does the number of voxels in tomographic phantoms. Therefore, comparing analytical versus voxelized phantoms, which in this context can be generalized for tomographic phantoms of any kind, in terms of computational speed is related to comparing the costs of solving a large number of linear equations to solving a much smaller number of nonlinear equations.

A. Ray-Tracing of Voxelized Phantoms

One of the first “fast” ray-tracing approaches dedicated for use in medical imaging for calculating the exact locations of the intersections of a line with the voxel boundaries of a 3-D array is Siddon’s well-known algorithm [17]. Based on the fact that the voxel boundaries constitute an orthogonal set of equally spaced parallel planes in space, the original cuboid-ray intersection problem can be transformed into a plane-ray intersection problem reducing the computational time scale from N^3 to $3N$. Following Siddon’s model, Han *et al.* [28] further propose acceleration of the original approach by replacing multiplicative operations with straightforward index assignment operations taking the orientation of the photon path to the array grid into account. This modified algorithm leads to approximately a 70% decrease in computational time compared with Siddon’s original algorithm.

Ray-tracing algorithms described previously generally do not take the object model into consideration and, therefore, result in computational costs that are independent from the phantom data being traced and depend only on the dimension of the array N . Based on the assumption that adjacent voxels often have identical descriptive parameters (material, activity value), alternative algorithms have been proposed that modify the object description of voxelized phantoms with the objective to reduce the number of intersection calculations. Taking the given regional parametric uniformity of phantoms into account, Ogawa *et al.* developed algorithms that perform on octree representation of phantom objects [29], [30] and, in an extended octree approach, on maximum rectangular region (MRR) object description [31], [32]. Compared with an (unspecified) voxel-based method, the authors report a 54% decrease in simulation time of the MRR method when applied on the MCAT phantom [32]. Because the computational performance of these approaches depends on the object shapes of the phantoms, we can expect higher speed-up ratios for simple-geometry analytically defined phantoms (67% decrease in computational load is reported for a cylinder phantom), but in the case of true segmented tomographic data, lower gains should be expected as the phantom regions become more complicated in shape.

In order to calculate ray intersections with tomographic phantoms, we use a modified version of Siddon’s algorithm that is similar to the algorithm proposed in [28]. The algorithm first calculates all intersections of the photon path with the (x, y, z) planes that define the boundaries of the voxels as described in [28]. The number of calculated intersections per photon path lies in the range $1 \dots 384$ for 128^3 and $1 \dots 786$ for 256^3 voxels, depending on the initial emission point and the orientation of the path vector to the phantom cuboid. A modification to further speed the simulation was implemented based on the piecewise homogeneity of the array data. As the photon path intersects the voxel grid, consecutive voxels along the path often have identical material or activity values associated with them. Thus, it is not necessary to include boundary intersections of voxels into the subsequent calculation of photon probabilities when no change in associated value occurs along the ray. With this modification, the number of intersecting points of the photon path with planes representing material or activity boundaries

is reduced significantly compared with the number of intersections of the path ray with the voxel enclosing planes. Optimally, the modified ray-tracing algorithm returns the same number of intersecting points as those returned number of intersection points of the photon path with analytically defined simploid shapes, given the same relative orientation of the photon ray to the phantom surfaces. Practically, this is offset by the number of intersections caused by the discretization problem discussed in Section III-B.

B. Ray-Tracing of Superquadric-Based Phantoms

Derived by extending the parameterization of their standard-form quadratic surfaces, superellipsoids and supertoroids have been proposed as primitives for shape representation [33], [34]. Because of their several and advantageously unusual properties, superquadrics are ideally suited to phantom modeling. They have closed-form algebraic expressions for their most important geometric features. Their implicit descriptions are all satisfied by solution of a generalized equation $F(x, y, z) = 0$, which determines where a given point $[x, y, z]^T$ is located relative to the surface. The intersections of a photon path with a superquadric surface can be found by substituting the vector expression of the parametric ray equation, given by

$$\left. \begin{aligned} x &= x_0 + t_x d \\ y &= y_0 + t_y d \\ z &= z_0 + t_z d \end{aligned} \right\} \Rightarrow \xi = \xi_0 + t d, \quad (1)$$

into the implicit surface (“inside-outside”) function, in the case of a superellipsoid, given by

$$F_E(x, y, z) = \left(\left| \frac{x}{a_1} \right|^{2/\epsilon_2} + \left| \frac{y}{a_2} \right|^{2/\epsilon_2} \right)^{\epsilon_2/\epsilon_1} + \left| \frac{z}{a_3} \right|^{2/\epsilon_1} - 1, \quad (2)$$

where a_1 , a_2 , and a_3 define superquadric radii upon the x -, y -, and z -axes, respectively. The parameters ϵ_1 and ϵ_2 , by which each trigonometric function is raised to an exponent, define squareness of the shape in the z -axis and in the x - y -plane, respectively. When both ϵ_1 and ϵ_2 are one, (2) defines an ellipsoid or, if $a_1 = a_2 = a_3$, a sphere. The implicit surface function of the superquadric toroid is given by

$$F_T(x, y, z) = \left| \left(\left| \frac{x}{a_1} \right|^{2/\epsilon_2} + \left| \frac{y}{a_2} \right|^{2/\epsilon_2} \right)^{\epsilon_2/2} - a_4 \right|^{2/\epsilon_1} + \left| \frac{z}{a_3} \right|^{2/\epsilon_1} - 1, \quad (3)$$

with a_4 being the hole parameter. Substituting (1) into (2) or (3) results in a polynomial of variable order (depending on ϵ_1 and ϵ_2) in the ray parameter d , which is proportional to the distance along the ray at which the intersections occur.

Solving the polynomial of a “real” superquadric requires numerical root finding approaches, such as *regula falsi* or the secant method [35], to determine the intersections of the photon

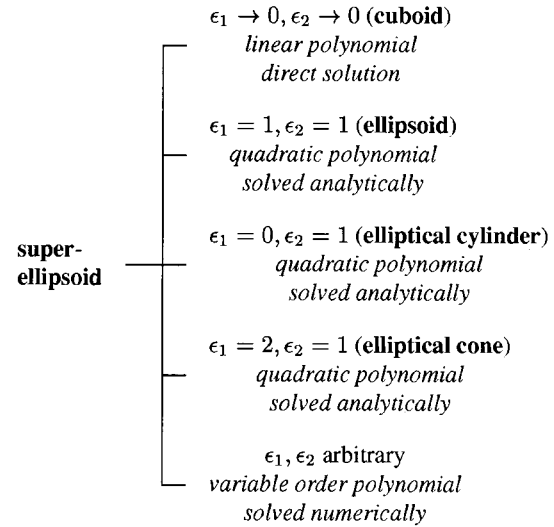


Fig. 4. Classification of superellipsoid cases and implemented algorithms [35], [36] for calculation of ray-surface intersections.

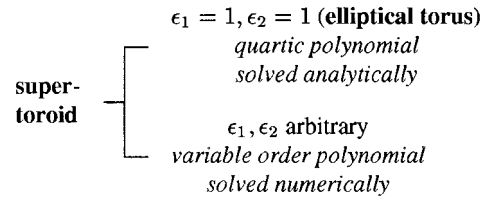


Fig. 5. Classification of supertoroid cases and implemented algorithms [35], [37] for calculation of ray-surface intersections.

ray with a phantom object. Although we have observed that the implemented root-finding algorithms proceed very fast because the problem is mostly well conditioned (convergence is often reached after four to six iterations), solving the special cases of linear, quadratic, and quartic polynomials by their appropriate analytical or direct methods has been implemented according to Figs. 4 and 5 and leads to significantly faster solutions. As we can see in Fig. 4, all forms of quadratic simploids that have been used to define the surfaces of the MCAT phantom as well as the quadrics in references [18], [25], [26] are special cases of superellipsoid shapes. This means in turn that superquadric-based phantom models are natural extensions of those phantoms. Fig. 5 lists supertoroid cases and implemented algorithms.

Computational times necessary to calculate 100 000 emitted photon histories simulated in an analytical phantom consisting only of a single superquadric solid per simulation indicate variations in time with object shape (Fig. 6). Photons are sampled inside the corresponding solid, whereby no scattering has been included in any case. The values clearly indicate a decrease in computational time when special intersection cases of superquadrics are solved with appropriate algorithms, taking into account the order of the polynomial for which the roots have to be found. All data provided in this paper have been derived from Monte Carlo simulations coded in C and performed on a PentiumII/450-MHz PC running Linux, but the variations should be similar in relative magnitude on different platforms.

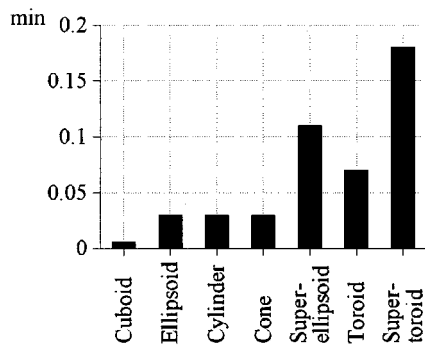


Fig. 6. Computational time requirements (total Monte Carlo simulation) for 100 000 ray-solid intersection calculations shown for classified shapes of the superquadric-based phantom model.

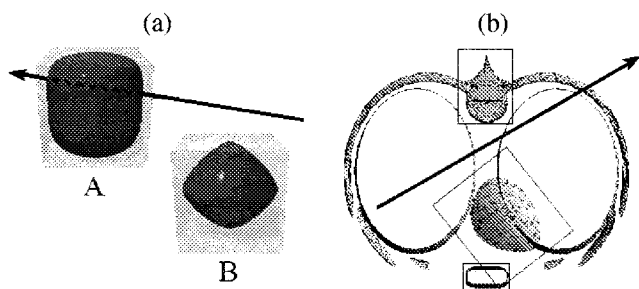


Fig. 7. Implemented ray rejection tests: (a) solid-based (solid B is rejected); (b) group-based (grouped are sternum, heart, and vertebra, which in this case rejects nonlinear ray-solid intersection calculations of 15 shapes). Bounds on groups represent maximal sizes of those objects that may occur at different transverse levels.

C. Local Rejection Testing

Assuming that a photon ray intersects only a small number of phantom solids per traveling path, a fast and efficient rejection test for eliminating unnecessary ray-solid intersection calculations has been implemented based on the fact that every surface lies entirely within the cuboid defined by the surface radii a_1 , a_2 , and a_3 . Those cuboid intersections are calculated before and serve as initial values for the more expensive ray-solid intersection calculation, which simplifies and accelerates the numerical root finding by bracketing the root. Because of this solid-based ray rejection technique, nonlinear polynomials only have to be solved if the ray intersects the surrounding cuboid, as shown in Fig. 7(a). As an extension of this, the same principle has been implemented to reject a ray from every surface, which is part of an ensemble of surfaces modeling a greater structure or organ [Fig. 7(b)].

The higher the order of polynomials of rejected shapes, the more effective are the applied ray rejection tests. For an ellipsoid, the solid-based ray rejection test adds 20% of computational time if the ray intersects the solid surrounding cuboid, but saves 80% of the time needed to solve the quadratic polynomial in case the ray does not intersect the ellipsoid. In case the solid is a superellipsoid, the overhead—neglecting faster convergence by bracketing the root—is only 5.5% compared with 94.5% increase in efficiency if no root exists.

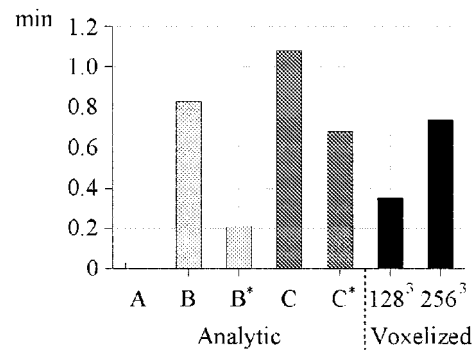


Fig. 8. Time requirements of Monte Carlo simulations for 100 000 histories (without scatter) depending on phantom design and representation. Analytical phantom representation: (A) point source phantom; (B) cold rod:sphere phantom; (C) superquadric anthropomorphic thorax phantom; as well as voxelized representations (independent of phantom content). Asterisks indicates same phantom with ray-tracing and group-based rejection test.

D. Comparison of Analytical and Voxelized Phantoms

As previously mentioned, in contrast to voxelized phantoms, computational time for analytical phantom simulations depends on the number, location, and types of the phantom solids. For example, phantoms shown in Fig. 1 representing well-known examples of possible superquadric-based phantom designs have been compared regarding their effect on computational speed (Fig. 8). All values are based on 100 000 photon histories for each simulation. Because computational times do not differ noticeably for simulations employing any of the voxelized phantom representations discussed here, the times shown in Fig. 8 represent average values for all experiments based on voxelized phantoms with a corresponding number of voxels. Simulation of the cold rod:sphere phantom results in computational times shown in Fig. 8 B and B*, where B* is the simulation after the solids of the phantom have been grouped into seven subsets. Although the subset grouping was not optimized (regions have been defined based on logical subsets of rods and spheres), the decrease of computational load is significant and results in a 3.5 times faster Monte Carlo simulation than compared with the voxelized phantom containing 256^3 voxels.

The superquadric male anthropomorphic thorax phantom (Fig. 8 C and C*) has been designed to be used in a Tc-99m MIBI myocardial perfusion SPECT simulation; i.e., activity has been assigned in the myocardium, lungs, liver, gall-bladder, spleen, and kidneys. Although the number of solids is significantly less than is the number of solids in the cold rod:sphere phantom, most of the surfaces of the anthropomorphic phantom are true superquadrics or toroids that require more extensive intersection calculations resulting in longer simulation times than for the cold rod:sphere phantom. Also, the decrease of simulation time after additional solid grouping (solids are mainly grouped according to their organ type) is less than was seen for the cold rod:sphere phantom. Reasons for this can be found in that solids, like the rib torus's, the lung bodies, and the liver superquadrics, are large in size and intersected very often. Additionally, a significant number of photons is emitted

inside the myocardium, for instance, and will, therefore, intersect many of the shapes on which the heart is modeled. This again indicates the dependency of the analytical phantom compartments on computational speed.

For the different phantoms compared in this section, Monte Carlo simulations performed on analytically defined phantoms with both types of ray-rejection implemented are faster than are those performed on voxelized phantoms with 256^3 voxels; simple geometric phantoms such as point source or the cold rod: sphere phantom performed significantly faster compared with their voxelized representations with 128^3 voxels as well. Although computational cost is certainly an important factor in favoring one method over another, especially if high statistic simulation times are measured in days, the accuracy of the phantom model plays an important role as well. The analytical model can take advantage of both of these requirements.

V. SPECT SIMULATIONS

The most important aspect in comparing analytical versus voxelized phantom representation for Monte Carlo simulation includes the quality of the results. After discussing discretization problems (Section III), here we focus on whether those errors are visible in reconstructed SPECT images. Because the conclusions of this investigation should be valid for all phantom representations shown in Fig. 1, we will concentrate on SPECT simulations of the cold rod: sphere phantom (Fig. 1, center).

Spatial image resolution of both, 128^3 and 256^3 , voxelized phantom representations (Section II) is higher than is the intrinsic resolution of the SPECT system modeled (3.6 mm). Fig. 9 shows reconstructed images of Monte Carlo simulated projections using the following parameters (identical for all simulations): 500 000 generated unscattered photon histories (140.5 keV) per projection, 120 projections, 128×128 bins per projection; a parallel hole collimator with 40.0-cm square extent, 4.0 cm thickness, 0.15-cm hole size, and a septal thickness of 0.02 cm; radius of rotation is 15.0 cm; projection data have been reconstructed with five iterations of ordered subset expectation maximization (OSEM) and are uniformly attenuation corrected. A visual comparison of Fig. 9(a), which shows the reconstruction of the simulation using the analytical phantom, with Fig. 9(b) and (c), demonstrates that the (smallest) rods can be slightly better distinguished with simulation conditions (a) and (b). However, the detailed profiles in Fig. 10 seem to contradict this observation. As characterized by cold-rod-to-background contrast and cold-rod widths, the closest agreement of the profile to the true phantom geometry seems to be given by the profile representing the voxelized phantom with 128^3 voxels. This profile has significantly exaggerated extreme compared with the profiles of the other results in Fig. 9 that are similar (despite statistics). Obviously, this cannot be the case. A look at the cross-sectional view of the voxelized phantom representations at the profile location (Fig. 11) reveals the reason for the misleading interpretation of the simulation results.

The three Monte Carlo simulations of the cold rod: sphere phantom modeling the same imaging system generate equally accurate results—applied on and with respect to three different

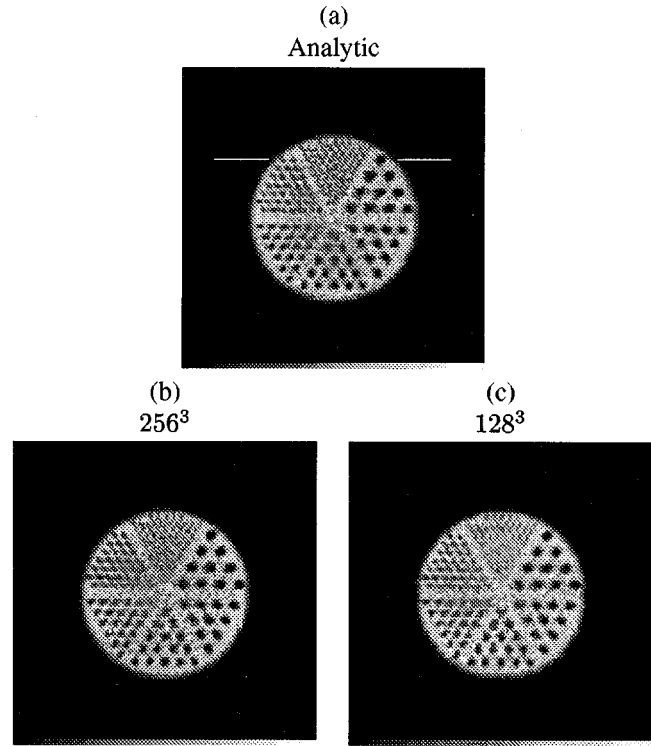


Fig. 9. Reconstructed images (20 slices are added together in the rods section) of Monte Carlo simulated projections using (a) analytical phantom (lines indicate location of profiles shown in Fig. 10), (b) 256^3 , and (c) 128^3 voxelized phantoms.

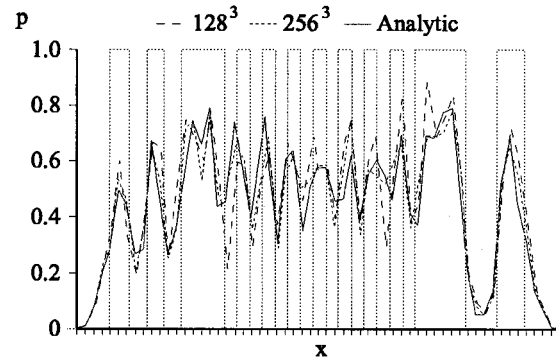


Fig. 10. Profiles of the images shown in Fig. 9 (see text). Also marked is the extracted true (unsampled) phantom profile at the corresponding location.

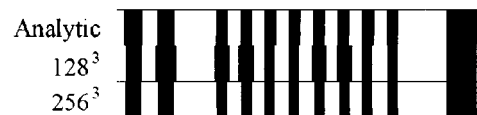


Fig. 11. Cross-sectional view of analytic (reflects true object description) and the voxelized phantom representations at profile location. Black sections indicate discretized cold rods that have larger volumes in the 128^3 phantom compared with the 256^3 phantom. White sections represent the emission activity distribution.

phantoms. This example underlines that discretization errors are prevalent in reconstructed images because of a rearrangement of the count densities and material properties in the simulated objects. Discretization errors can only be minimized if the phantom resolution is chosen higher than is the resolution of the

imaging system or potentially if there is a change in the activity densities to account for the volume differentials. Moreover, recalculating the activity distribution increases the complexity of the simulation setup because the distributions can no longer be considered uniform. These problems are entirely avoided with “true” analytical phantoms. Adapting the finer sampling principle to voxelized phantoms results in a larger number of data voxels and subsequently results in increased computational costs.

VI. CONCLUSION

As we have shown in the previous sections, analytical phantoms generate only a fraction of computational costs than voxelized phantoms do in terms of memory allocation. Calculation time of analytically defined phantoms, however, depends on the number of objects modeled, which in the case of highly complex phantoms can result in more expensive ray-tracing calculations compared with voxelized object representations. Besides (negligible) precision limitations through the data type used, analytical phantoms do not have discretization errors that result in inaccurate simulation results compared with the actual phantom geometry. The finer the spatial resolution of the discretized phantom compared with those of the imaging system under simulation, the smaller the influence of discretization errors on simulated projection data and, subsequently, their visibility in the reconstructed images. This comes with an associated computational cost.

An advantage of analytical phantoms is that they can be defined in a straightforward manner. True tomographic phantoms based on segmented CT or MRI data, on the other hand, should be used to more accurately approximate detailed human shapes (true-to-human geometry) and clinically realistic source distributions. Although such phantoms have been shown to be more appropriate if the effects of complex protuberances between internal organ structures are under investigation, the analytical phantoms offer advantages in (computational) time and accuracy for evaluation and investigation of imaging physics and reconstruction algorithms in a straightforward and efficient manner.

REFERENCES

- [1] D. Reaside, “Monte Carlo principles and applications,” *Phys. Med. Biol.*, vol. 21, no. 2, pp. 181–197, 1976.
- [2] P. Andreo, “Monte Carlo techniques in medical radiation physics,” *Phys. Med. Biol.*, vol. 36, no. 7, pp. 861–920, 1991.
- [3] H. Zaidi, “Relevance of accurate Monte Carlo modeling in nuclear medical imaging,” *Med. Phys.*, vol. 26, no. 4, pp. 574–608, 1999.
- [4] M. Ljungberg and S. Strand, “Attenuation and scatter correction in SPECT for sources in a nonhomogeneous object: A Monte Carlo study,” *J. Nucl. Med.*, vol. 32, no. 6, pp. 1278–1284, 1991.
- [5] R. Jaszcak, C. Floyd, S. Manglos, K. Greer, and R. F. Coleman, “Cone beam collimation for single photon emission computed tomography: Analysis, simulation, and image reconstruction using filtered backprojection,” *Med. Phys.*, vol. 13, no. 4, pp. 484–489, 1986.
- [6] C. Floyd, R. Jaszcak, C. Harris, K. Greer, and R. Coleman, “Monte Carlo evaluation of Compton scatter subtraction in single photon emission computed tomography,” *Med. Phys.*, vol. 12, no. 6, pp. 776–778, 1985.
- [7] C. Tung and G. Gullberg, “A simulation of emission and transmission noise propagation in cardiac SPECT imaging with nonuniform attenuation correction,” *Med. Phys.*, vol. 21, no. 10, pp. 1565–1576, 1994.
- [8] M. Ljungberg, M. King, G. Hademenos, and S. Strand, “Comparison of four scatter correction methods using Monte Carlo simulated source distributions,” *J. Nucl. Med.*, vol. 35, no. 1, pp. 143–151, 1994.
- [9] J. Luo, K. Koral, M. Ljungberg, and C. Floyd, Jr., “A Monte Carlo investigation of dual-energy-window scatter correction for volume-of-interest quantification in Tc-99m SPECT,” *Phys. Med. Biol.*, vol. 40, pp. 181–199, 1995.
- [10] P. MacKowen, *Stochastic Simulation in Physics*. New York: Springer, 1997.
- [11] G. Zubal and C. Harrell, “Voxel based Monte Carlo calculations of nuclear medicine images and applied variance reduction techniques,” in *Inform. Process. Med. Imag., 12th Int. Conf.*, 1991, pp. 23–33.
- [12] F. Beekman, H. Dejong, and E. Slijpen, “Efficient SPECT scatter calculation in nonuniform media using correlated Monte Carlo simulation,” *Phys. Med. Biol.*, vol. 44, pp. N183–N192, 1999.
- [13] E. Hoffman, P. Cutler, W. Digby, and J. Mazziotto, “3-D phantom to simulate cerebral blood flow and metabolic images for pet,” *IEEE Trans. Nucl. Sci.*, vol. 37, no. 2, pp. 616–620, 1990.
- [14] G. Zubal, C. Harrell, E. Smith, Z. Rattner, G. Gindi, and P. Hoffer, “Computerized three-dimensional segmented human anatomy,” *Med. Phys.*, vol. 21, no. 2, pp. 299–302, 1994.
- [15] B. Tsui, J. Terry, and G. Gullberg, “Evaluation of cardiac cone-beam SPECT using observer performance experiments and ROC analysis,” *Investigative Radiology*, vol. 28, no. 12, pp. 1101–1112, 1993.
- [16] X. Zhao, B. Tsui, G. Gregoriou, D. Lalush, J. Li, and R. Eisner, “Evaluation of corrective reconstruction methods using a 3D cardiac-torso phantom and bull’s-eye plots,” *IEEE Trans. Nucl. Sci.*, vol. 41, no. 6, pp. 2831–2837, 1994.
- [17] R. Siddon, “Fast calculation of the exact path for a three-dimensional CT array,” *Med. Phys.*, vol. 12, pp. 252–255, Mar./Apr. 1985.
- [18] H. Wang, R. Jaszcak, and R. Coleman, “Solid geometry-based object model for Monte Carlo simulated emission and transmission tomographic imaging systems,” *IEEE Trans. Med. Imag.*, vol. 11, pp. 361–372, Mar. 1992.
- [19] J. Peter, R. Jaszcak, and R. Coleman, “Composite quadric-based object model for SPECT Monte Carlo simulation,” *J. Nucl. Med.*, vol. 39, no. 5 (suppl.), p. 121, 1998.
- [20] R. Pretorius, W. Xia, M. King, B. Tsui, T. Pan, and B. Villegas, “Evaluation of right and left ventricular volume and ejection fraction using a mathematical cardiac torso phantom,” *J. Nucl. Med.*, vol. 38, pp. 1528–1535, 1997.
- [21] J. Peter, D. Gilland, R. Jaszcak, and R. Coleman, “Four-dimensional superquadric-based cardiac phantom for Monte Carlo simulation of radiological imaging systems,” *IEEE Trans. Nucl. Sci.*, to be published.
- [22] D. Kadrmas, E. Frey, S. Karimi, and B. Tsui, “Fast implementations of reconstruction-based scatter compensation in fully 3D SPECT image reconstruction,” *Phys. Med. Biol.*, vol. 43, pp. 857–873, 1998.
- [23] A. Welch, A. Smith, and G. Gullberg, “An investigation of the effect of finite system resolution and photon noise on the bias and precision of dynamic cardiac SPECT parameters,” *Med. Phys.*, vol. 22, no. 11, pp. 1829–1836, 1995.
- [24] E. Frey and B. Tsui, “Modeling the scatter response function in inhomogeneous scattering media for SPECT,” *IEEE Trans. Nucl. Sci.*, vol. 41, no. 4, pp. 1585–1593, 1994.
- [25] H. Wang, R. Jaszcak, D. Gilland, K. Greer, and R. Coleman, “Solid geometry based modeling of nonuniform attenuation and Compton scattering in objects for SPECT imaging systems,” *IEEE Trans. Nucl. Sci.*, vol. 40, no. 4, pp. 1305–1312, 1993.
- [26] H. Wang, R. Jaszcak, and R. Coleman, “A new composite model of objects for Monte Carlo simulation of radiological imaging,” *Phys. Med. Biol.*, vol. 38, pp. 1235–1262, 1993.
- [27] C. Bai, L. Zeng, I. Laurette, V. Panin, and G. Gullberg, “A study of intensity decrease of apical region in cardiac spect images,” in *Proc. 1999 Int. Mtg. Fully 3D Image Reconstruction Radiol. Nucl. Med.*, 1999, pp. 293–296.
- [28] G. Han, Z. Liang, and J. You, “A fast ray-tracing technique for TCT and ECT studies,” in *Proc. IEEE Nucl. Sci. Symp. Med. Imag. Conf.*, 1999, pp. M10–75.
- [29] K. Ogawa and S. Maeda, “A Monte Carlo method using octree structure in photon and electron transport,” *IEEE Trans. Nucl. Sci.*, vol. 42, no. 6, pp. 2322–2326, 1995.
- [30] K. Ogawa, S. Takahashi, and Y. Satori, “Description of an object in Monte Carlo simulations,” *IEEE Trans. Nucl. Sci.*, vol. 44, no. 4, pp. 1521–1526, 1997.
- [31] R. Sato and K. Ogawa, “New accelerating method for photon transport in Monte Carlo simulation,” in *Proc. IEEE Nucl. Sci. Symp. Med. Imag. Conf.*, 1998, pp. M10–165.

- [32] R. Suganuma and K. Ogawa, "Object description by a maximum rectangular method in Monte Carlo simulation," in *Proc. IEEE Nucl. Sci. Symp. Med. Imag. Conf.*, 1999, pp. M3–82.
- [33] A. Barr, "Superquadrics and angle-preserving transformations," *IEEE Comput. Graphics Applicat.*, vol. CGA-1, no. 1, pp. 11–23, 1981.
- [34] A. Pentland, "Perceptual organization and the representation of natural form," *Artif. Intell.*, vol. 28, pp. 293–331, 1986.
- [35] W. Press, S. Teukolsky, W. Vetterling, and B. Flannery, *Numerical Recipes in C: The Art of Scientific Computing*. Cambridge, U.K.: Cambridge Univ. Press, 1992.
- [36] J. Cychosz and W. Waggenspack, "Intersecting a ray with a quadric surface," in *Graphics Gems*, D. Kirk, Ed. New York: Academic Press, 1992, vol. III, pp. 275–283.
- [37] J. Cychosz, "Intersecting a ray with an elliptical torus," in *Graphics Gems*, J. Arvo, Ed. New York: Academic Press, 1991, vol. II, pp. 251–256.